

Impedance spectroscopy characterization of c-Si solar cells with SiO_x/Poly-Si rear passivating contacts

Mohamed M. Shehata^{a,b,*}, Thien N. Truong^a, Rabin Basnet^a, Hieu T. Nguyen^a, Daniel H. Macdonald^a, Lachlan E. Black^{a,**}

^a School of Engineering, The Australian National University, Canberra, ACT 2600, Australia

^b Department of Physics, Faculty of Science, Minia University, El Minya City, 61519, Egypt

ARTICLE INFO

Keywords:

c-Si solar cell
Impedance spectroscopy
High-efficiency
Passivating contact
Poly-Si/SiO_x
Carrier lifetime
Cole-Cole plot

ABSTRACT

Impedance spectroscopy (IS) is a powerful characterization technique that is commonly applied to organic, perovskite, and thin-film solar cells. However, it has not been widely applied to solar cells based on crystalline silicon (c-Si), which is by far the most relevant commercial technology, and particularly not to modern, high-efficiency silicon devices. In this work, we demonstrate the application of the IS technique to a 21.25% efficient c-Si solar cell featuring SiO_x/poly-Si rear passivating contacts. This type of cell architecture is structurally similar to that of current high-efficiency industrial devices. The investigated cell was measured over a wide range of frequencies under illuminated open-circuit conditions and under different DC biases in darkness. The resistive and capacitive components associated with the p⁺-n junction and at n⁺-poly-n low-high junction, which cannot be resolved by standard DC measurements, are readily distinguished by the IS method. These parameters allowed for the determination of junction time constants and lifetimes. We find that the lifetimes derived from IS measurements performed under open-circuit illuminated conditions are in excellent agreement with the carrier recombination lifetime under illumination. Our findings demonstrate that IS is a promising technique to explore various dynamic properties of high-efficiency c-Si solar cells.

1. Introduction

To aid in the development of novel photovoltaic technologies and device architectures and to maximize photovoltaic efficiency, precise measurements of solar cell characteristic parameters are critical. In general, it is beneficial to perform both dynamic and static measurements of photovoltaic devices in order to obtain a comprehensive insight into their performance and to assist in the design of efficient and reliable devices. DC characterization measures parameters such as power conversion efficiency η , open-circuit voltage V_{oc} , short-circuit current density J_{sc} , fill factor FF , series resistance R_s , shunt resistance R_{sh} , and ideality factor. Meanwhile, the AC dynamic approach provides information on the capacitance and dynamic resistance of solar cells. These parameters are vital for optimizing the performance of power converters [1]. For example, the capacitance of the solar cell affects the photovoltaic regulators' performance [1]. These must operate at a high frequency, which raises the switching regulators' ripple voltage owing to

the capacitance of the solar cells [2]. Meanwhile, the dynamic resistance value is important for modeling the solar power system and ensuring stability [3]. Knowing these parameters is also important to deliver consistent power to the load at the proper voltage and current, since solar panels are typically interfaced with their loads through an electronic power conditioner and a battery [4]. We highlight a published review article that provides a thorough discussion of methodologies and strategies for determining the dynamic characteristics of solar cells and their applications [5].

Solar cells are DC-operating devices, but, due to their design, they have a complex impedance. As a result, the impedance spectroscopy (IS) technique can be utilized to investigate their dynamic characteristics. IS is a powerful, non-destructive characterization technique that can be applied to finished devices [6–8] or modules. IS is carried out by applying an alternating voltage to a sample and measuring the amplitude and phase shift of the current response. Therefore, the real and imaginary parts of the impedance of the sample can be measured as a

* Corresponding author. School of Engineering, The Australian National University, Canberra, ACT 2600, Australia.

** Corresponding author.

E-mail addresses: mohamed.ismael@anu.edu.au, mohamed.shehata@mu.edu.eg (M.M. Shehata), lachlan.black@anu.edu.au (L.E. Black).

function of frequency. These impedances can be fit using an electrical equivalent circuit to extract the dynamic physical characteristics of a solar cell or module. IS has emerged as an effective characterization technique for photovoltaic devices, as demonstrated in the literature [9]. This technique has also received considerable attention within the academic community, and it has been widely used to investigate organic [10], perovskite [11,12], dye-sensitized [13], and other thin-film [14, 15] solar cells. However, it has been applied comparatively infrequently to c-Si solar cells, despite the fact that they make up the vast majority of commercial devices and are therefore of great technological interest.

Previous applications of the IS technique to c-Si cells have focused on relatively low-efficiency heterojunction or homojunction cells, mostly based on the now-outdated Al-back-surface-field (Al-BSF) technology. For example, Mora-Seró et al. applied the IS technique to 13.4–14.1% efficient c-Si solar cells with a-Si:H heterojunctions and directly metallized Al rear contacts [16]. The carrier lifetime was determined from IS measurements under illuminated open-circuit conditions. Almora et al. used a similar approach to evaluate the carrier lifetime in 13.4–15.6% efficient c-Si solar cells with MoO₃ and V₂O₅ heterojunctions and a-SiC_x:H rear passivation/contact layers [17]. The IS technique has also been used to investigate homojunction (n⁺-p-p⁺) c-Si solar cells based on the Al-BSF concept, with efficiencies of 17.4% [18], and 14.83% [19]. IS also appears to be a promising method for characterizing degradation mechanisms in silicon solar cell modules [20]. In an interesting recent degradation study, modules of bifacial monocrystalline silicon passivated emitter and rear cells (p-PERC) were monitored using IS in conjunction with other characterization techniques under damp heat exposure and various applied voltages [21].

Despite these previous works, there are no reports of the IS approach

being applied to high-efficiency (i.e., >20%) c-Si solar cells based on SiO_x/poly-Si passivating contacts, which are now being employed in the latest generation of high-efficiency commercial c-Si solar cells [22]. Passivating contacts are a new technology that comprise a set of layers that enable both selective conduction of charge carriers and effective passivation for silicon surfaces [23,24]. Such SiO_x/poly-Si passivating contacts have been widely investigated in recent years to suppress rear-contact recombination losses [25], leading to some of the highest efficiencies reported for c-Si solar cells [26,27]. The highest reported efficiency for such devices is 26.0%, which was obtained for a structure with an n⁺-poly-Si/SiO_x/c-Si contact on the rear side of a p-type c-Si base [28]. These cells are now starting to be applied in industry to boost efficiency beyond the limits of the current mainstream PERC (Passivated Emitter and Rear Cell) technology [29,30].

Therefore, in this paper, we apply impedance spectroscopy (IS) for the first time to characterize high-efficiency (~21.3%) c-Si solar cells based on SiO_x/poly-Si rear passivating contacts. IS measurements are performed as a function of applied bias in darkness and under illuminated open-circuit conditions. In addition, current density–voltage (J–V) in the dark and under varying illumination intensity, and dark capacitance–voltage (C–V) characteristics are also measured. Such high-efficiency devices are expected to yield well-defined impedance characteristics with standard Cole–Cole plots that are quite near to theory, which is an advantage in this respect. We analyze and compare the J–V, C–V, and IS results, and use them to quantify the static and dynamic properties of the studied c-Si solar cell. We seek to establish what can and cannot be learned from IS characterization of such high-efficiency c-Si devices in order to help guide the design and optimization of high-efficiency c-Si solar cells.

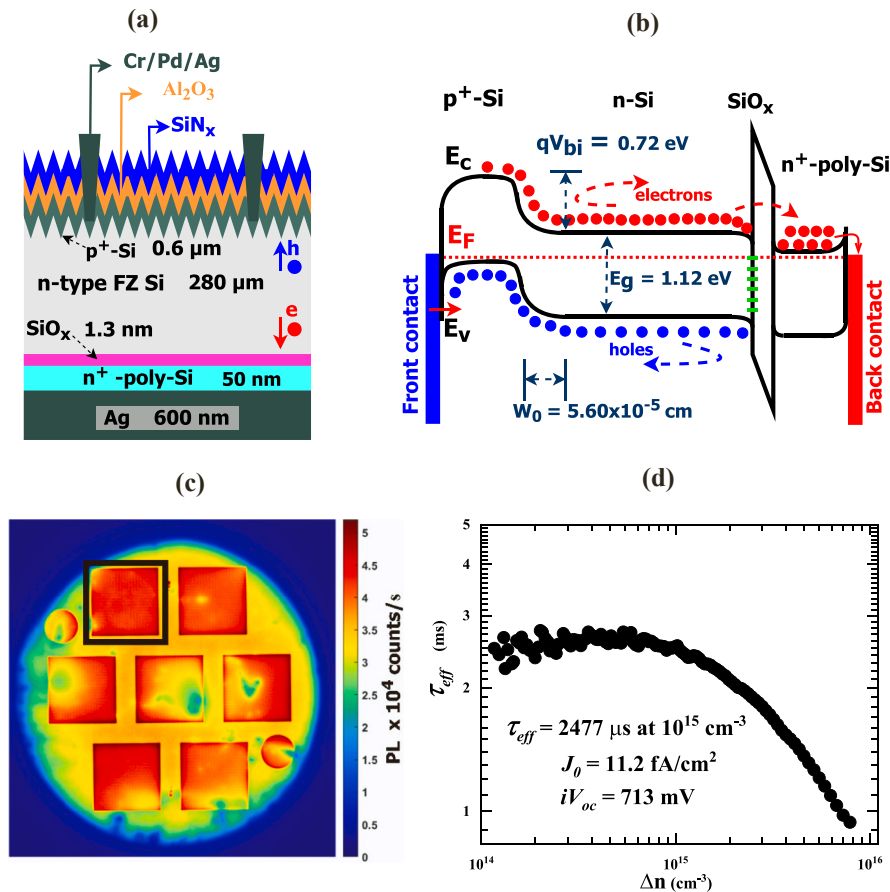


Fig. 1. (a) Structural diagram of examined poly-Si/SiO_x c-Si solar cell. (b) Corresponding schematic energy band diagram under equilibrium conditions. (c, d) Photoluminescence image (The cell with the black-labeled square was the subject of this study.) and effective minority carrier lifetime versus minority carrier density of the 4-inch cell precursors after all high-temperature steps (before metallization), respectively.

2. Experimental section

n-type float-zone (FZ) silicon wafers with a thickness of $\sim 280 \mu\text{m}$ and a bulk resistivity of $2 \Omega \text{ cm}$ were used to fabricate $2 \times 2 \text{ cm}^2$ cells. The detailed cell structure and schematic energy band diagram at equilibrium (interpreted in supplementary information) are shown in Fig. 1(a) and Fig. 1(b), respectively. A homogenous p^+ emitter was formed on the textured front side by boron diffusion performed at 930°C (20 min deposition, 25 min post-oxidation, 20 min drive-in) resulting in a sheet resistance $R_{\text{sheet}} = 130\text{--}140 \Omega/\square$. The rear-side passivating contact was achieved by the growth of an ultrathin ($\sim 1.3 \text{ nm}$) chemical SiO_x layer [31], followed by the deposition of an intrinsic amorphous silicon layer ($\sim 50 \text{ nm}$ thick) by plasma-enhanced chemical vapor deposition (PECVD) (Roth & Rau AK400). The amorphous silicon layer was then simultaneously doped and crystallized to n^+ -poly-Si in a tube furnace at 820°C for 25 min with a 30 min drive-in, using phosphorus oxychloride (POCl_3) as a dopant source. For front surface passivation, Al_2O_3 was deposited using atomic layer deposition (Beneq TFS 200), and capped by a SiN_x antireflection coating layer deposited using plasma-enhanced chemical vapor deposition (PECVD). The front metal contact grid was defined by photolithography and a Cr/Pd/Ag contact stack was deposited by thermal evaporation and lift-off. The rear metal contact was formed by evaporating a uniform 600 nm thick layer of silver. Both front and rear contacts were subjected to silver electroplating to thicken the contacts. Finally, sintering was performed at 300°C in forming gas (5% H_2 :95% N_2) for 10 min. The resulting front-contact fingers had a width of $13\text{--}14 \mu\text{m}$, resulting in cell-area shading of $\sim 1.7\%$. Additional details on the solar cell fabrication process can be found in Ref. [31]. Photoluminescence (PL) imaging was performed using a LIS-R1 PL imaging tool from BT imaging [32] and the surface passivation was characterized using a Sinton Instruments WCT-120 photoconductance lifetime tester. Fig. 1(c and d) displays the PL image and the surface passivation performance following all high-temperature processes and prior to metallization. Before the metallization step, the average lifetime of the fabricated cells (τ_{eff}) is $2477 \mu\text{s}$ with recombination current density prefactor J_0 of 11.2 fA/cm^2 and implied-open circuit voltage iV_{oc} of 713 mV . The cell with the black-labeled square was the subject of this study.

Current-density-voltage (J-V) and Suns- V_{oc} measurements were performed in-house using an FCT-450 tool from Sinton instruments at standard test conditions. Impedance spectroscopy (IS) and the capacitance-voltage (C-V) measurements were performed at room temperature using a computer-controlled Keysight B1500A Semiconductor Device Analyzer with B1520A multi-frequency capacitance measurement unit (MFCMU). The impedance was measured as a function of frequency from 1 kHz to 1 MHz , with an AC perturbation signal of 10 mV . The measured impedance was fitted using the EIS Spectrum Analyzer software [33]. This is a stand-alone program for analyzing and simulating impedance spectra and has been used before in the literature [34,35]. The fitting error between the theoretical fit model and experimental data was around $10^{-3}\%$. It is worth noting that sister cells were tested by IS and similar behaviors were obtained. The active dopant profiles for the emitter (p^+ -Si region) and rear contact (SiO_x/n^+ -poly-Si region) were measured by the electrochemical capacitance-voltage (ECV) method using a WEP Wafer Profiler CVP21.

3. Results and discussion

3.1. DC characteristics

Prior to presenting IS results, we first present the standard DC characterization of the device. Fig. (2) shows the dark current-voltage (I-V) characteristics of the device under negative and positive DC biases at room temperature. It can be seen that the device follows a classical diode behavior in the dark with a knee voltage (cut-in or threshold voltage) $V_{\text{knee}} = 0.63 \text{ V}$. The total DC resistance R_{DC} of the cell was

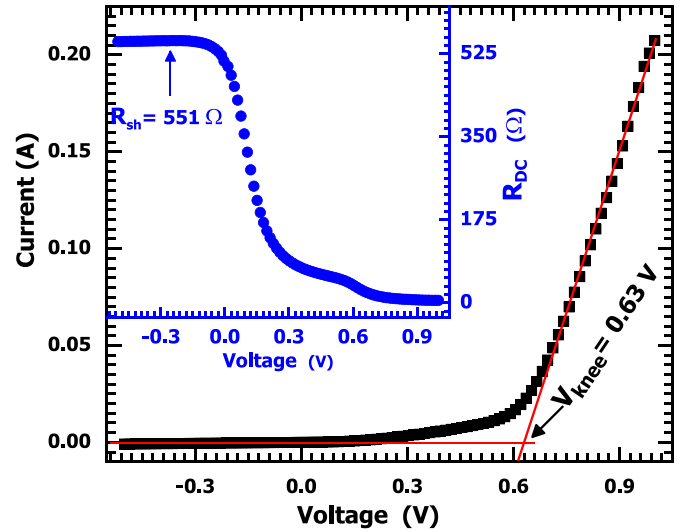


Fig. 2. Dark current-voltage characteristics of $\text{SiO}_x/\text{poly-Si}$ c-Si solar cell at 25°C . Inset: the total solar cell resistance as a function of applied voltage.

obtained by taking the derivative of voltage V with respect to current I , $R_{\text{DC}} = \partial V / \partial I$. The variation of R_{DC} as a function of the applied voltage V is shown in the inset of Fig. (2). It decreases with increasing forward bias (FB) and saturates in the reverse bias (RB) region, where it is approximately equal to the shunt resistance R_{sh} [18], resulting in $R_{\text{sh}} = 551 \Omega$. This relatively low shunt resistance will affect the fill factor, open-circuit voltage, and efficiency of the device, particularly at lower illumination intensities. Illuminated current density-voltage (J-V) measurements at illumination intensities ranging from 0.2 to 1 Sun (AM1.5G spectrum) at 25°C and their corresponding output power curves are shown in Fig. 3 (a) and Fig. 3 (b), respectively. The resulting efficiency is $\eta = 21.25\%$ at 1 Sun, with an open-circuit voltage $V_{\text{oc}} = 670 \text{ mV}$, a short circuit current $J_{\text{sc}} = 41.2 \text{ mA/cm}^2$, and a fill factor $FF = 76.2\%$. The lower V_{oc} of the investigated device is partly a consequence of the thicker absorber ($\sim 280 \mu\text{m}$) used in these laboratory cells compared to industrial devices (this alone accounts for $\sim 14 \text{ mV}$ difference when comparing to a $160 \mu\text{m}$ thick cell). The determined photovoltaic parameters under different illumination intensities are listed in Table 1.

In order to allow comparison between the excess minority carrier lifetime corresponding to open-circuit conditions and the lifetime values calculated from the impedance spectroscopy analysis (discussed in section 3.3) the former lifetime was calculated from standard Suns- V_{oc} measurements of the open-circuit voltage as a function of slowly varying illumination intensity [36]. Assuming no trapping occurs in the base, we have $\Delta n = \Delta p$, and the excess carrier concentration Δn can be calculated from V_{oc} according to [37]

$$V_{\text{oc}} = \frac{k_B T}{q} \ln \left[\frac{(N + \Delta n) \Delta n}{n_{i,\text{eff}}^2} \right] \quad (1)$$

where $k_B T / q$ is the thermal voltage, N is the doping concentration and is equal to $2.84 \times 10^{15} \text{ cm}^{-3}$ (calculated from the wafer resistivity of $1.6 \Omega \text{ cm}$ measured by the photoconductance method), and $n_{i,\text{eff}}$ is the effective intrinsic carrier concentration, which we calculate from the expression of [38] at 25°C ($8.30 \times 10^9 \text{ cm}^{-3}$) together with the bandgap narrowing model of [39]. The excess carrier lifetime τ as a function of Δn is given by [36]

$$\tau = \frac{\Delta n}{G - d\Delta n/dt} \quad (2)$$

where G is the rate of generation and can also be determined from [37].

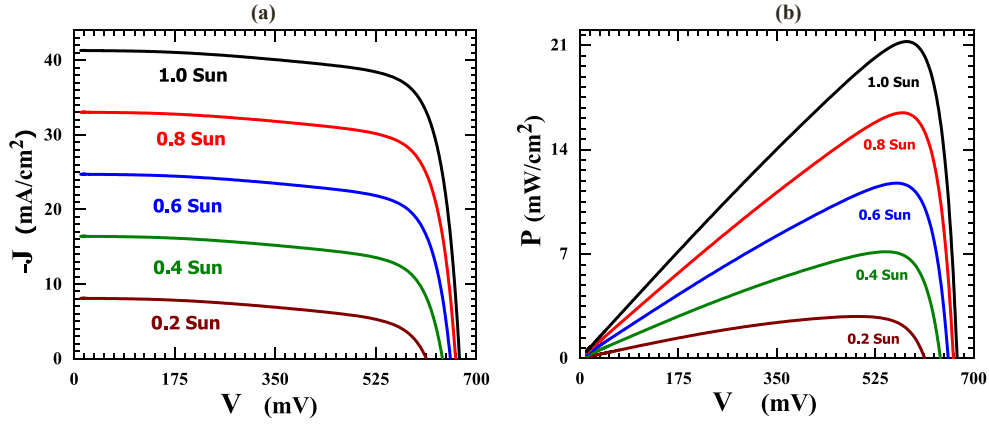


Fig. 3. (a) Experimental current-density-voltage curves of SiO_x/poly-Si c-Si solar cell measured at a range of illumination levels (given in units of Suns) using solar simulator at 25 °C. (b) Corresponding output power.

Table 1

Photovoltaic parameters of the studied poly-Si/SiO_x c-Si solar cell under different illumination levels at 25 °C.

Parameter (units)	0.2 Suns	0.4 Sun	0.6 Sun	0.8 Sun	1.0 Sun
V _{oc} (mV)	612	640	654	663	670
J _{sc} (mA/cm ²)	8.08	16.39	24.70	33.02	41.20
P _{mp} (mW/cm ²)	2.81	7.15	11.75	16.47	21.24
V _{mp} (mV)	492	541	563	574	580
J _{mp} (mA/cm ²)	5.72	13.20	20.86	28.69	36.57
FF (%)	56.90	68.10	72.70	75.20	76.90
η (%)	14.06	17.80	19.57	20.56	21.25

$$G = \frac{J_{gen}}{qW} \quad (3)$$

where W is the thickness of the silicon wafer, and J_{gen} is the generation current density, which is determined by multiplying J_{sc} measured at one sun illumination by the illumination intensity in suns, measured as a function of time using a calibrated reference cell. The variation of excess carrier lifetime τ and concentration Δn with the open-circuit voltage V_{oc} at 298 K are shown in Fig. (4). τ initially increases with V_{oc} , reaching a maximum value of 348 μ s at $V_{oc} = 645$ mV ($\Delta n = 1.4 \times 10^{15}$ cm⁻³), before again decreasing. The latter decrease is likely linked to the onset of significant Auger recombination as well as increasing surface

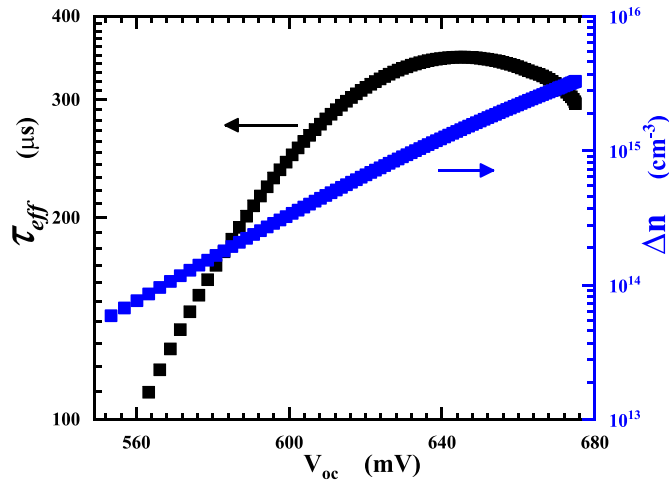


Fig. 4. Variation of minority carrier lifetime τ and excess minority carrier concentration Δn with the open-circuit voltage of the SiO_x/poly-Si c-Si solar cell, determined from Suns- V_{oc} measurements at 25 °C.

recombination as the carrier concentration increases in the intermediate injection range.

3.2. Capacitance-voltage characteristics

The doping profiles for the emitter (p⁺-Si) and the poly-Si contact are shown in Fig. 5(a and b), respectively. While the active phosphorus concentration in n⁺-poly-Si is roughly 3×10^{20} cm⁻³, the emitter carrier concentration is around 2×10^{19} cm⁻³. Whereas the donor concentration in the poly-Si is plateaued up to 0.04 μ m and exponential decline indicates the establishment of a diffused region in the c-Si substrate beyond the SiO_x tunneling layer, the emitter carrier concentration drops suddenly at 0.4 μ m, indicating the formation of an electrically abrupt junction with the n-type c-Si substrate. In addition, the cell's C-V response was measured in the dark at room temperature to obtain information about the nature of the junction, its built-in potential, the substrate dopant concentration, and the depletion region width. A high measurement frequency of 500 kHz was chosen in these measurements to avoid any contribution from the interface states. These mostly cannot follow the AC signal at high frequency and consequently don't contribute considerably to the measured capacitance [40]. The reverse-biased depletion capacitance C_{dl} is given by Ref. [41]:

$$C_{dl} \propto (V_{bi} + V_R)^{-n} \text{ or } C_{dl} \propto (V_R)^{-n} \text{ for } (V_R \gg V_{bi}) \quad (4)$$

where $n = 1/3$ for a linearly graded junction and $n = 1/2$ for a one-sided abrupt junction. V_R is the reversed applied DC bias. A logarithmic plot of C_{dl} versus V_R is depicted in Fig. 5(a). The relation can be fit by a straight line with a slope of $n = 0.49$, indicating that an electrically abrupt pn junction is formed between the p⁺-Si emitter and n-Si base. The magnitude of the band-bending across the p⁺-Si/n-Si junction is given by the built-in potential V_{bi} . For a one-sided abrupt junction, V_{bi} can be determined using the Mott-Schottky relation between depletion capacitance C_{dl} and the applied voltage V [41]:

$$\frac{1}{C_{dl}^2} = \frac{2}{q\epsilon_{Si}\epsilon_o A^2 N} (V_{bi} - V - 2k_B T/q) \quad (5)$$

where q is the elementary charge, ϵ_{Si} the Si dielectric constant, ϵ_o is the permittivity of free space, V the applied bias, N is the donor carrier concentration in the base (n-Si), k_B is the Boltzmann constant, A is the cell area and T is the absolute temperature. The variation of C_{dl}^{-2} with the applied bias V is shown in Fig. 5(b). The doping concentration N was calculated from the slope of this plot, according to

$$N = \frac{2}{q\epsilon_{Si}\epsilon_o A^2} \left(\frac{d(C_{dl}^{-2})}{d(V)} \right) \quad (6)$$

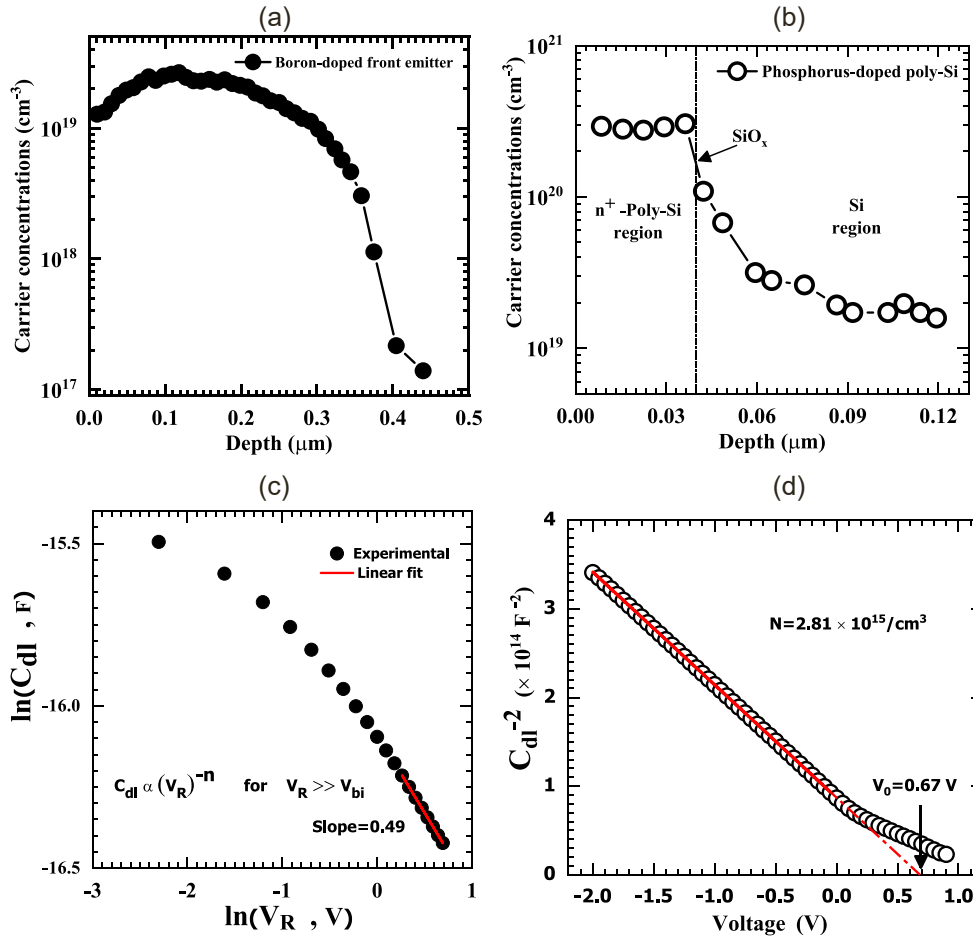


Fig. 5. (a,b) Dopant concentrations by ECV measurements for front emitter and rear poly-Si, respectively. (c) Log-log plot of depletion capacitance C_{dl} versus reverse bias (under dark and room temperature conditions) of the SiO_x/poly-Si c-Si solar cell, a straight line with a slope of 0.49 indicates an electrically abrupt pn junction between p⁺-Si emitter and n-Si base. (d) Experimental (symbols) Mott-Schottky plot with linear fit (red line) used to determine the substrate dopant concentration. (For interpretation of the references to colour in this figure legend, the reader is referred to the Web version of this article.)

Additionally, the built-in potential V_{bi} was determined from the corresponding intercept at $C_{dl}^{-2} = 0$ as

$$V_{bi} = V_0 + 2k_B T/q \quad (7)$$

where V_0 is the intercept of C_{dl}^{-2} with the voltage axis. The depletion region width under zero bias W_0 between the p⁺-Si and n-Si regions can be determined from the following equation [17]:

$$W_0 = \sqrt{\frac{2\epsilon_{Si}\epsilon_0}{qN} (V_{bi} - 2k_B T/q)} \quad (8)$$

Note that the correction factor $2k_B T/q$, which is sometimes neglected, has been included in Eqs. (5), (7) and (8) for greater accuracy [17, 41]. This correction factor $2k_B T/q$ is attributed, respectively, to the contributions of impurities and the tails of the majority carrier profiles in the n and p regions [41]. From the Mott-Schottky analysis we obtained a value of $N = 2.81 \times 10^{15} \text{ cm}^{-3}$, which is consistent with the value determined from the resistivity measured by photoconductance ($N = 2.84 \times 10^{15} \text{ cm}^{-3}$). Furthermore, the obtained value of the built-in potential ($V_{bi} = 0.72 \text{ eV}$), is consistent with the range of values previously reported for standard c-Si solar cells of 0.6 V–0.77 V [18,42,43]. The measured $W_0 = 5.60 \times 10^{-5} \text{ cm}$ from C–V data is also in reasonable agreement with the value obtained from IS measurements (see Fig. 7(a) at zero bias).

3.3. AC characteristics

The main objective of this study is to interpret the experimental IS measurements of a c-Si solar cell with a SiO_x/poly-Si rear passivating

contact. Based on the measured characteristics, we wish to determine the dynamic properties of the studied cell via IS analysis, including values of resistive and capacitive elements, and lifetimes under DC bias and illuminated open-circuit conditions. We will begin by explaining in detail the interpretation of the AC measurements of the investigated cell in terms of Cole–Cole plots. **These plots are complex-plane descriptions of the imaginary part of impedance response, or reactance Z'' (y-axis), as a function of the real part of impedance, or resistance Z' (x-axis) for different measured frequencies.** Fig. 6 shows a selection of the experimental Cole–Cole spectra for the studied c-Si solar cell under various DC biases in the dark, where the symbols and the lines show the experimental data and the theoretical fits, respectively. Note that Cole–Cole plots for the full range of measured biases in the dark are shown in Fig. S1 (supplementary information). **In the Cole–Cole plots, the solar cell exhibits a single semicircle with a unique time constant, whose diameter is strongly dependent on the applied DC bias.** These data have been modeled by the simple electrical equivalent circuit (EEC) shown in Fig. 6(a), which consists of a resistor R_s in series with the parallel combination of a resistance R_{p^+-n} and constant phase element (CPE_{p^+-n}). The complex impedance of the latter combination is given by [44]

$$Z^* = \left(\frac{1}{R_{p^+-n}} + \frac{1}{Z_{CPE_{p^+-n}}^*} \right)^{-1} \quad (9)$$

where the impedance of the constant phase element (CPE_{p^+-n}) is defined as follows:

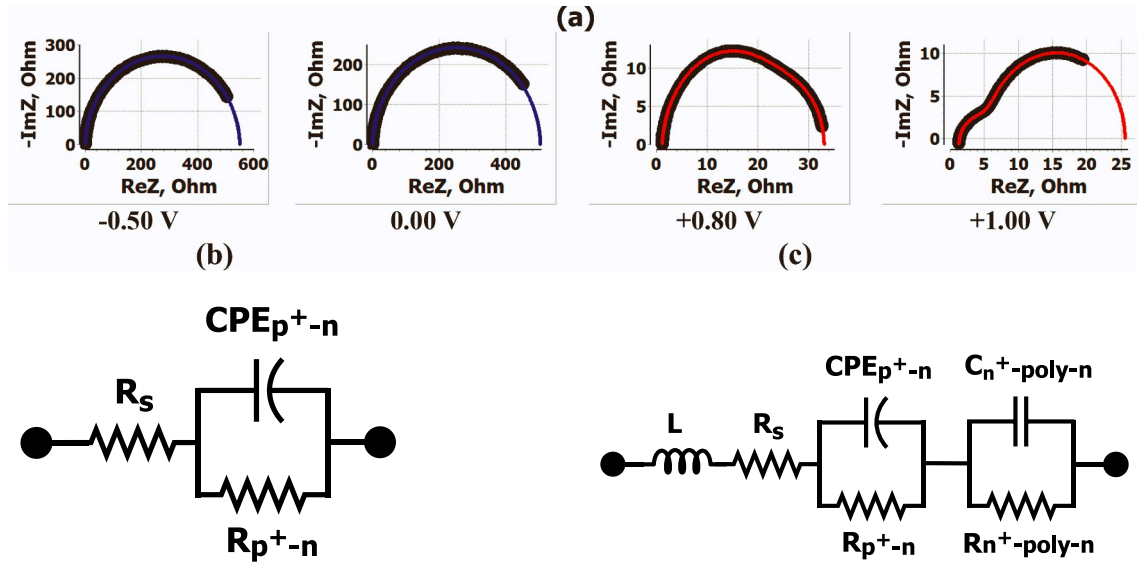


Fig. 6. (a) Room-temperature experimental Cole–Cole plots (symbols), and their corresponding fits (blue/red solid line) at different applied DC-biases of the SiO_x /poly-Si c-Si solar cell under dark conditions. (b,c) AC electrical equivalent circuit models used to fit the impedance measurements. (For interpretation of the references to colour in this figure legend, the reader is referred to the Web version of this article.)

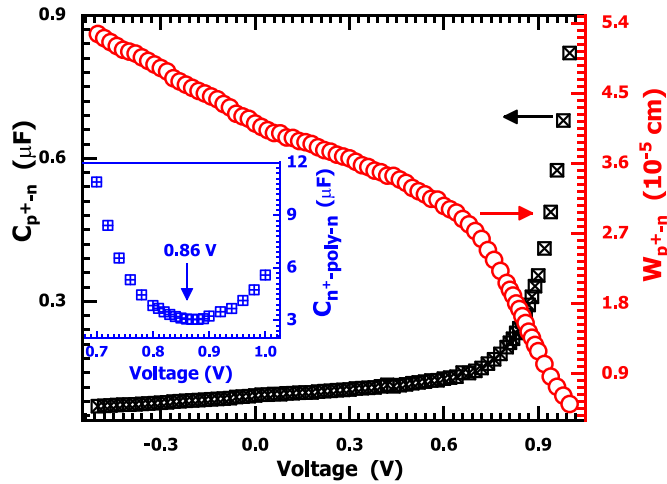


Fig. 7. Capacitance and depletion-region width of p^+-n junction of the SiO_x /poly-Si c-Si solar cell at different biases under dark and room-temperature conditions. Inset: the variation of low-high junction capacitance (at the interface between n^+ -poly-Si and n-Si) at high DC-bias.

$$\frac{1}{Z_{CPE_{p^+-n}}^*} = P(i\omega)^n \quad (10)$$

Where i is the imaginary unit, ω is the angular frequency, P is the magnitude of the CPE_{p^+-n} , and the exponent n describes the degree of the capacitive nature of the component. A CPE is considered a pure capacitor only when $n = 1$ (and a pure resistor when $n = 0$) [45]. From equations (9) and (10) the real Z' and imaginary Z'' parts of complex impedance can be stated as follows

$$Z' = R_s + \frac{R_{p^+-n}(1 + R_{p^+-n}P\omega^n \cos(n\frac{\pi}{2}))}{1 + 2R_{p^+-n}P\omega^n \cos(n\frac{\pi}{2}) + (R_{p^+-n}P\omega^n)^2} \quad (11)$$

$$Z'' = \frac{R_{p^+-n}^2 P\omega^n \sin(n\frac{\pi}{2})}{1 + 2R_{p^+-n}P\omega^n \cos(n\frac{\pi}{2}) + (R_{p^+-n}P\omega^n)^2} \quad (12)$$

As shown in Fig. 6 and Fig. S1 (Supplementary Information), the

model provides a perfect fit (blue line) for a variety of applied biases in dark conditions. The R_s in the EEC represents the resistance of the wires, front and rear contacts, and silicon bulk, and corresponds to the high-frequency intersection of the semicircle with the Z' -axis. The series resistance remains small ($<1 \Omega$) during the measurements, which means that there is no major degradation in the rear/front contacts of the sample [20]. The resistance R_{p^+-n} corresponds to the diameter of the semicircle and decreases in response to increasing the applied DC bias. R_{p^+-n} is attributed to the resistance, and CPE_{p^+-n} the capacitance, associated with the p^+-n junction. The decline in Cole–Cole spectra radii reflects the increase in space-charge-region (SCR) conductivity at the p^+-n junction, while the resistance contribution associated with the $n^+-poly-n$ low-high junction (LHJ) formed by the $n^+-poly-Si/SiO_x/n-Si$ rear contact is nearly negligible (a similar trend was observed previously for c-Si solar cells based on Al-BSF [6]). This increase in conductivity is mainly dominated by the increase of concentration of excess carriers produced through electrical injection at the electrodes under bias.

A second partial arc is clearly visible for data at high positive DC bias, as shown in Fig. 6 and Fig. S1 (Supplementary Information), in line with previous studies of n^+-p-p^+ Si solar cells by Refs. [19,42,46–48]. Due to the presence of two partial semicircular arcs, a more complex equivalent circuit model is required to fit the impedance spectra. Fig. 6(b), presents a model for the modified EEC of the investigated c-Si solar cell that takes into account the two partial arcs; where the fitting is represented by the red-line as shown in Fig. 6 and Fig. S1 (supplementary information) and then the Z' and Z'' relations of this EEC can be expressed as

$$Z' = \omega L + R_s + \frac{R_{p^+-n}(1 + R_{p^+-n}P\omega^n \cos(n\frac{\pi}{2}))}{1 + 2R_{p^+-n}P\omega^n \cos(n\frac{\pi}{2}) + (R_{p^+-n}P\omega^n)^2} + \frac{R_{n^+-poly-n}}{1 + (\omega R_{n^+-poly-n} C_{n^+-poly-n})^2} \quad (13)$$

$$Z'' = \frac{R_{p^+-n}^2 P\omega^n \sin(n\frac{\pi}{2})}{1 + 2R_{p^+-n}P\omega^n \cos(n\frac{\pi}{2}) + (R_{p^+-n}P\omega^n)^2} + \frac{\omega R_{n^+-poly-n} R_{n^+-poly-n} C_{n^+-poly-n}}{1 + (\omega R_{n^+-poly-n} C_{n^+-poly-n})^2} \quad (14)$$

where ωL denotes the inductive reactance of the probes and wires used for measurement (which also becomes non-negligible at high DC bias), $R_{n^+-poly-n}$ is the low-high junction resistance, and $C_{n^+-poly-n}$ is the low-

high junction capacitance. As can be seen, there is a perfect overlap between experimental data and EEC models. This confirms that the suggested EEC configurations are suitable to describe the impedance data over the whole examined frequency and bias range. The existence of these standard semicircles of the Cole–Cole plots implies that the studied solar cells have an ideal electrical response, no degradation, and stability [7] during the measurements. The observation of the parasitic inductive tail in the Cole–Cole plots at high frequencies is ascribed to stray inductance originating from the cables and electrodes [19]. The relative contribution from this component becomes non-negligible as the cell resistance decreases with increasing DC bias. Thus, it is necessary to add a series inductance L to the EEC (presented in Fig. 6(b)) in order to obtain a more accurate fit of impedance data. The value of L was found to be around 5×10^{-7} H for all measurements.

The second arc is represented by a parallel resistance and capacitance combination, which we attribute to the resistive and capacitive components of the formed low-high junction (LHJ) at the n^+ -poly-Si/SiO_x/n-Si interface under a high DC bias, and therefore designate $R_{n^+-poly-n}$ and $C_{n^+-poly-n}$. The transition from one to two separate time constants implies that IS results depend strongly on the applied DC bias. Note that the time $\tau = RC$ is the time constant defining the RC circuit. This is the charging/discharging period of the capacitor for the circuit in electronics. For impedance measurements of physical systems, such as silicon solar cells, time constants refer to the relaxation response of cell junctions to an externally applied oscillating electric field. For example, the junction depletion region of a solar cell is located between two conductive regions, the emitter and the base, and is analogous to dielectric material between two conductive electrodes. Therefore, the number of semicircles in the Cole–Cole plots of a cell indicates the number of junctions or Schottky contacts in this cell. The Cole–Cole plot should contain a few semicircles if the time constants are distinct while if the time constants are comparable, the semicircles will overlap and just one semicircle will be detected [9]. In addition, in the case of the solar cell under forward bias (and/or illumination), the relevant physical relaxation response is the recombination of injected excess carriers.

The contribution of this LHJ in the Cole–Cole spectrum is not observed in RB and/or moderate FB, but only when a strong FB (approximately 0.7 V) is applied (supplementary information S1). This is because the time constants of the p^+ -n junction and LHJ are similar at RB and moderate FB, resulting in the Cole–Cole plot displaying a singular semicircle with a single time constant. Since the LHJ is also comparatively thin compared to both the p^+ -n junction and the solar cell base, the total impedance at low FB is mainly dominated by the much larger impedance of the p^+ -n junction. At a stronger DC bias (0.7 V), the LHJ impedance becomes roughly comparable to the p^+ -n junction impedance because the latter is reduced. This allows the LHJ contribution in the Cole–Cole plots to be distinguished, similar to previous observations of n^+ -p- p^+ c-Si solar cells [19,42,46–48].

The influence of illumination, temperature, and applied bias on the LHJ contribution have previously been examined in detail via impedance spectroscopy for n^+ -p- p^+ c-Si solar cells with a then-conventional Al-diffused p-p+ “back-surface field” (BSF), in Refs. [19,42,46–48]. The contribution of the LHJ to the impedance of the examined c-Si solar cell with SiO_x/poly-Si rear passivating contact can be explained as follows. Firstly, the onset of a detectable BSF contribution for n^+ -p- p^+ c-Si solar cells has previously been observed in the range of $0.3 \text{ V} < V < 0.6 \text{ V}$ and appeared at the high-frequency region on the left-hand side of the Cole–Cole plots [19,42,46–48]. In contrast, the LHJ contribution observed in this study was detected above the knee voltage, i.e. $V \geq 0.7 \text{ V}$, and in the low-frequency region on the right-hand side of the Cole–Cole plots. This may be due to the device structure and the presence of the SiO_x/n⁺-poly-Si rear passivating contact.

Returning to the use of a constant phase element (CPE) instead of a real capacitor in the EEC, this is often used to describe interfaces that exhibit a wide distribution of relaxation times or are inhomogeneous

[45,49]. It was also found that a CPE provides a significantly better fit than using a simple capacitor in our case. The mathematical description and the physical interpretation of CPE are described in Ref. [44]. For $n < 1$, the real junction capacitance C_{p^+-n} at the p^+ -n junction can be calculated according to [44]

$$C_{p^+-n} = (P \times R)^{1/n} / R \quad (15)$$

The depletion region width for the p^+ -n junction, W_{p^+-n} , can be determined as a function of C_{p^+-n} according to [50]

$$W_{p^+-n} = \frac{\epsilon_0 \epsilon_{Si} A}{C_{p^+-n}} \quad (16)$$

where ϵ_0 is the permittivity of free space, ϵ_{Si} is the relative dielectric constant of Si (11.9) [41], and A is the cell area. Fig. 7(a) shows the variation of C_{p^+-n} and W_{p^+-n} under different DC biases (dark condition). These plots explain how the p^+ -n junction of the studied c-Si solar cell is influenced by the injection of charge carriers. Theoretically, two types of capacitances emerge in a pn junction diode: transition capacitance (C_T) and diffusion capacitance (C_D). Therefore, the measured junction capacitance using IS [46] is $C_j = C_D + C_T$, where C_T is also known as the space-charge-region (SCR) capacitance (or depletion-region capacitance) and can be determined by the Mott–Schottky relation (mentioned in section 3.2 in this context). Indeed, as shown in Fig. S2 (Supplementary Information) the depletion region capacitance obtained from the IS analysis is quite similar to that acquired from C–V measurements, where the remaining difference can be attributed to neglect of the series resistance contribution in the C–V measurements. C_D is a combination of the diffusive components of the base C_{DB} and emitter C_{DE} [6,19]. In the RB and low FB regions, C_j is dominated by C_T [6]. In this region, the majority carriers are displaced from the pn junction. As a result, the width of the depletion region increases with decreasing applied bias. As the FB increases, the transition capacitance C_T becomes small compared to the diffusion capacitance C_D . In this region, electrons and holes will cross the depletion region and enter into the emitter and base, respectively. The accumulation of excess minority carriers near the depletion region edge will decrease W_{p^+-n} . Under strong FB, $C_j \approx C_D$, where C_D increases exponentially with V according to Ref. [18] $C_D = C_0 \exp(qV_b/mk_B T)$, where C_0 is a pre-exponent factor and is a voltage-independent constant and m is the diode ideality factor. In addition, the dependence of LHJ capacitance at high injection levels is represented in the inset of Fig. 7(a). The variation of $C_{n^+-poly-n}$ shows an inflection point at $V = 0.86 \text{ V}$. At the inflection point, (where $C_{n^+-poly-n}$ changes from decreasing to increasing with applied bias) the contributions of the p^+ -n junction and the n^+ -poly-n LHJ to the experimental impedance results are almost equivalent as shown in Fig. S1 (supplementary information).

The dependence of junction resistance R_{p^+-n} on the applied bias V is depicted in Fig. 8 (a). This plot illustrates the significant effect of applied voltage on the resistance R_{p^+-n} of the p^+ -n junction, and its behavior is qualitatively and quantitatively similar to that seen in DC experiments as illustrated in Fig. S3 (Supplementary Information). This demonstrates the measurement’s precision and the suggested EEC’s suitability for fitting the impedance data. In addition, under negative bias conditions, the solar cell junction resistance R_{p^+-n} provides the largest contribution to the impedance (Cole–Cole diameter), and this corresponds to the shunt resistance [42]. The determined shunt resistance, $R_{sh}(IS) = 550 \Omega$, obtained using IS analysis, is well matched to the value calculated from the dark current–voltage measurements, $R_{sh}(IV) = 551 \Omega$, in the RB region (shown in the inset of Fig. 2). The mutual agreement between IS and dark I–V also confirms the validity of the measurement. Fig. 8(a) also shows the variation of LHJ resistance $R_{n^+-poly-n}$ extracted from the low-frequency arc of the Cole–Cole plots as a function of bias. It is observed that $R_{n^+-poly-n}$ increases and saturates at strong FB. This may be due to the majority carrier concentration (electrons) on the base side

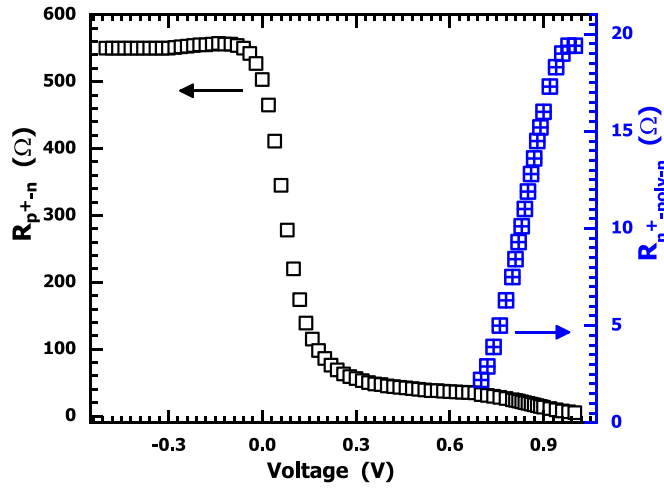


Fig. 8. p^+-n junction resistance and $n^+-poly-Si-n$ resistance as a function of applied bias (under dark and room-temperature conditions) of the $SiO_x/poly-Si$ c-Si solar cell.

of the SiO_x interface in the LHJ becoming comparable with the depleted electron concentration at the edge of donor concentration of the $n^+-poly-Si$ region. Moreover, the R_{p^+-n} and $R_{n^+-poly-n}$ values correspond to the diffusion resistance of the p^+-n junction and LHJ respectively at high DC bias [48].

The dependence of the time constant associated with the p^+-n junction ($R_{p^+-n} C_{p^+-n}$) and LHJ ($R_{n^+-poly-n} C_{n^+-poly-n}$) of the studied device as a function of applied bias is illustrated in Fig. 9(a). At $-0.5 \leq V \leq 0.0$ V, $R_{p^+-n} C_{p^+-n}$ is basically equal to $R_{SH} C_T$. This product has no physical meaning because the cell capacitance is dominated by the depletion region capacitance [48]. With growing FB, the diffusion of injected charge carriers plays a progressively greater role in governing p^+-n diode and LHJ electrical behaviors. According to IS analysis in previous reports [19,42,46–48], when the diffusion capacitance C_D governs the device capacitance, the carrier lifetime at the p^+-n junction and LHJ can be calculated, respectively, by $\tau_{p^+-n} = 2R_D C_D$ and $\tau_{n^+-poly-n} = 2R_{n^+-poly-n} C_{n^+-poly-n}$ (note that, in the $\tau_{n^+-poly-n}$ expression, the factor of 2 was added empirically to be in line with the functional form for τ_{p^+-n} [6]).

The variation of τ_{p^+-n} and $\tau_{n^+-poly-n}$ at high DC biases are illustrated in the inset of Fig. 9(b). It was observed that with the rise in applied bias, the junction lifetime τ_{p^+-n} decreased. In contrast, the LHJ lifetime $\tau_{n^+-poly-n}$ increases with increasing applied bias. By comparing the carrier lifetime for the p^+-n junction and LHJ of the investigated solar cell with those reported in previous studies of c-Si solar cells based on Al-BSF rear contacts, it was found that the p^+-n junction lifetime in the studied

cell (8–10 μ S) is less than the literature values (15–20 μ S). This is mainly because the examined device has a lower shunt resistance than previously reported devices. On the other hand, the carrier lifetime (40–230 μ S) associated with the $n^+-poly-n$ LHJ is much greater than the values obtained for Al-BSF devices (around 2 μ S) [19,42,46–48]. This is consistent with the lower surface recombination associated with $SiO_x/poly-Si$ passivating contacts and may explain in impedance analysis terms why these contacts outperform Al-BSF technology.

Furthermore, we performed IS measurements under illuminated open-circuit conditions. Fig. 10 shows the experimental Cole–Cole plots under these conditions. To accomplish this, a bias voltage identical to the open-circuit voltage V_{oc} was applied in the presence of illumination, thereby ensuring a more homogenous distribution of excess carriers in the device by suppressing DC current. As the Cole–Cole plots again display two semicircles in the high-frequency and low-frequency regions, the EEC in Fig. 6(b) was used to fit the measured Cole–Cole plots. In addition, Fig. S4 (supplementary information) illustrates basic equivalent circuit models and their corresponding Cole–Cole plots, demonstrating how to extract the equivalent circuit's components. The lifetime was determined using the fitting parameter values extracted from the equivalent circuit, and the variation of the lifetime as a function of the open-circuit voltage is illustrated in Fig. 10. The AC components corresponding to the high-frequency arc seem to be relatively potential-independent, with the resistance seen to decrease slightly with increasing irradiance in the range of 0.5–0.3 Ω . The lifetime of the high-frequency component was determined to be less than 2 μ s, while the lifetime of the low-frequency component has a maximum value of 387 μ s. Interestingly, the lifetime values associated with the low-frequency component are consistent with those determined using the Suns- V_{oc} approach, as shown in Fig. 11. Therefore, this lifetime can be considered as the recombination lifetime of the cell.

4. Conclusion

J–V, C–V, and IS characteristics of c-Si solar cells based on $SiO_x/poly-Si$ rear passivating contacts have been investigated and interpreted in this study. The efficiency of the examined c-Si solar cell is $\sim 21.3\%$, with an open-circuit voltage of 670 mV, a short circuit current of 41.20 mA/cm², and a fill factor of 76.90%. The ECV and C–V measurements confirmed the presence of a one-sided electrically abrupt p^+-n junction with built-in potential $V_{bi} = 0.72$ V, and base donor concentration $N = 2.81 \times 10^{15}$ cm⁻³. IS provides the AC equivalent circuit of the investigated c-Si solar cell as a function of injection level both in the dark and under illuminated open-circuit conditions. The lifetime associated with the p^+-n junction (8–10 μ s) of the investigated device under dark forward-bias conditions is lower than the values reported in the literature (15–20 μ s) for c-Si solar cells based on an Al-BSF, despite the higher open-circuit voltage of our device. This is mostly due to the fact that this

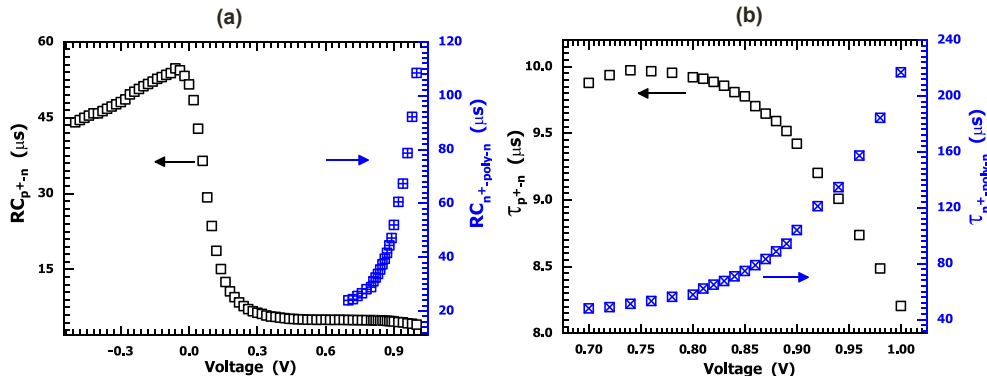


Fig. 9. (a) Time constants associated with the p^+-n and $n^+-poly-Si-n$ junctions as a function of bias (under dark and room-temperature conditions) for the $SiO_x/poly-Si$ c-Si solar cell. (b) Corresponding junction lifetimes at high DC biases.

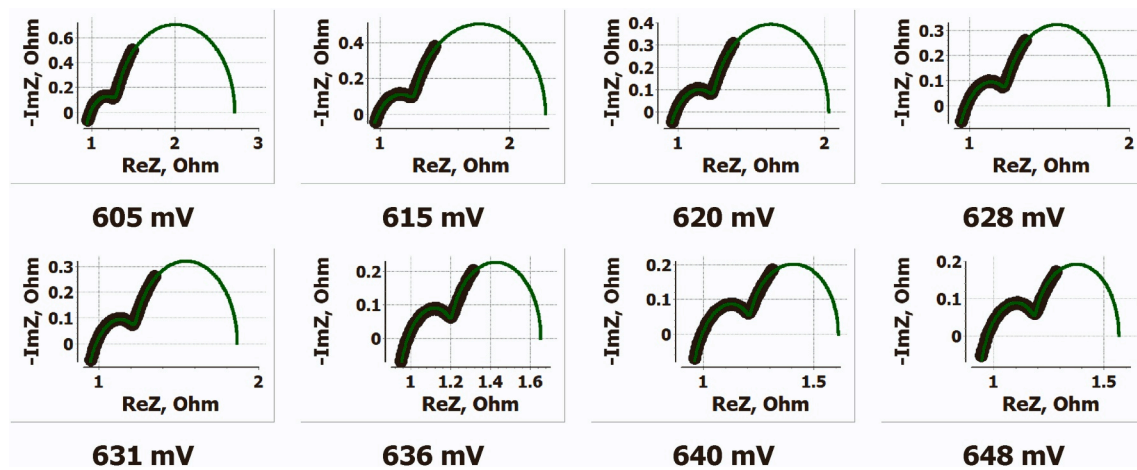


Fig. 10. Experimental Cole–Cole plots (black symbols), and their corresponding fits (green solid lines) measured at 25 °C as a function of illuminated open-circuit voltage for the SiO_x/poly-Si rear passivating contact c-Si solar cell. (For interpretation of the references to colour in this figure legend, the reader is referred to the Web version of this article.)

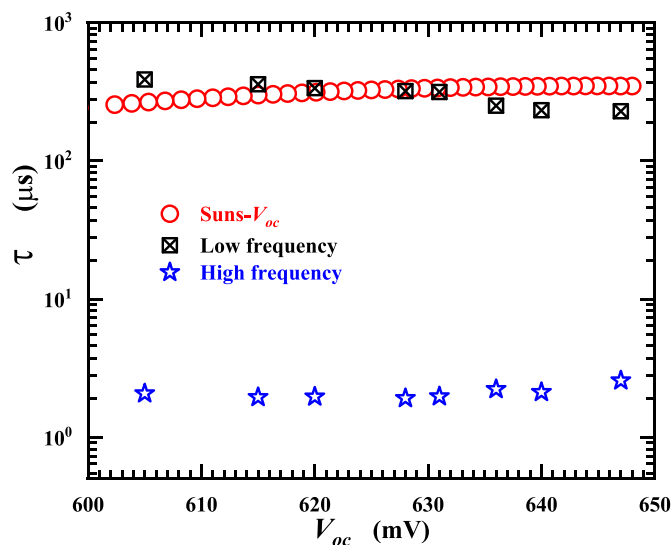


Fig. 11. Lifetime versus open-circuit voltage of the SiO_x/poly-Si c-Si solar cell, determined from the Suns- V_{oc} , low- and high-frequency components of impedance measurements performed at open-circuit voltage under variable illumination levels.

device has a lower shunt resistance than previously reported for Al-BSF-based devices. The carrier lifetime obtained using the IS technique under illuminated open-circuit conditions (387 μ s) is in excellent agreement with that obtained using the Suns- V_{oc} approach (370 μ s). In addition, an experimental approach for evaluating the impedance properties of the LHJ was demonstrated. The lifetime associated with the LHJ of the examined device (40–230 μ s) is significantly longer than the values published in the literature (about 2 μ s) for c-Si solar cells based on an Al-BSF structure. This might explain, in terms of impedance analysis, why SiO_x/poly-Si passivating contacts out-perform Al-BSF technology. Compared to the DC techniques usually applied to characterize complete c-Si solar cells (e.g. Illuminated Current–Voltage, Suns- V_{oc}), the IS technique has the following advantages: i) it allows direct measurement of the substrate dopant concentration in finished devices, ii) it directly provides the carrier recombination lifetime and excess carrier concentration, without requiring knowledge of the c-Si material properties (i.e. mobility, n_i) and their dependence on excess carrier concentration, doping and temperature (it can therefore also provide a means of measuring the latter properties), and iii) under certain conditions, it

allows the contributions of individual junctions within the device to be distinguished. The IS technique thus provides a comprehensive framework for assessing the impedance properties of the LHJ, which in turn can facilitate the task of efficient design of SiO_x/poly-Si contacts for high-performance c-Si solar cells.

CRediT authorship contribution statement

Mohamed M. Shehata: Software, Methodology, Investigation, Formal analysis, Conceptualization, Writing - original draft, Writing - review & editing. **Thien N. Truong:** Investigation, Methodology. **Rabin Basnet:** Investigation, Methodology. **Hieu T. Nguyen:** Investigation, Writing - review & editing. **Daniel H. Macdonald:** Project administration, Funding acquisition, Supervision, Writing - review & editing. **Lachlan E. Black:** Supervision, Conceptualization, Investigation, Project administration, Validation, Visualization, Writing - review & editing.

Declaration of competing interest

The authors declare that they have no known competing financial interests or personal relationships that could have appeared to influence the work reported in this paper.

Data availability

Data will be made available on request.

Acknowledgements

This work was supported by the Australian Renewable Energy Agency (ARENA) through project 2017/RND017. The authors would like to thank Drs. Fiona J. Beck and Daniel Walter for assisting with the measurement.

Appendix A. Supplementary data

Supplementary data to this article can be found online at <https://doi.org/10.1016/j.solmat.2022.112167>.

References

- [1] R.A. Kumar, M. Suresh, J. Nagaraju, Effect of solar array capacitance on the performance of switching shunt voltage regulator, *IEEE Trans. Power Electron.* 21 (2006) 543–548.

- [2] W. Kim, V.-H. Duong, T.-T. Nguyen, W. Choi, Analysis of the effects of inverter ripple current on a photovoltaic power system by using an AC impedance model of the solar cell, *Renew. Energy* 59 (2013) 150–157.
- [3] L. Qin, S. Xie, C. Yang, J. Cao, Dynamic model and dynamic characteristics of solar cell, *IEEE*, in: 2013 IEEE ECCE Asia Downunder, 2013, pp. 659–663.
- [4] R.A. Kumar, M. Suresh, J. Nagaraju, Measurement and comparison of AC parameters of silicon (BSR and BSFR) and gallium arsenide (GaAs/Ge) solar cells used in space applications, *Sol. Energy Mater. Sol. Cell.* 60 (2000) 155–166.
- [5] D. Cotfas, P. Cotfas, S. Kaplanis, Methods and techniques to determine the dynamic parameters of solar cells, *Renew. Sustain. Energy Rev.* 61 (2016) 213–221.
- [6] P. Yadav, K. Pandey, V. Bhatt, M. Kumar, J. Kim, Critical aspects of impedance spectroscopy in silicon solar cell characterization: a review, *Renew. Sustain. Energy Rev.* 76 (2017) 1562–1578.
- [7] M. Shehata, T. Abdel-Malik, K. Abdelhady, AC impedance spectroscopy on Al/p-Si/ZnTPyP/Au heterojunction for hybrid solar cell applications, *J. Alloys Compd.* 736 (2018) 225–235.
- [8] M. Makhlof, M. Shehata, Exploring illumination effect on the impedance spectroscopy and dielectric dispersion of 5, 10, 15, 20-tetrakis (4-methoxyphenyl)-21H, 23H-porphine cobalt (II)/silicon heterojunction photovoltaic, *J. Mater. Sci. Mater. Electron.* 31 (2020) 13970–13978.
- [9] E. Von Hauff, Impedance spectroscopy for emerging photovoltaics, *J. Phys. Chem. C* 123 (2019) 11329–11346.
- [10] B. Arredondo, B. Romero, G. Del Pozo, M. Sessler, C. Veit, U. Würfel, Impedance spectroscopy analysis of small molecule solution processed organic solar cell, *Sol. Energy Mater. Sol. Cell.* 128 (2014) 351–356.
- [11] L. Contreras-Bernal, S. Ramos-Terrón, A. Riquelme, P.P. Boix, J. Idigoras, I. Mora-Seró, J.A. Anta, Impedance analysis of perovskite solar cells: a case study, *J. Mater. Chem. B* 7 (2019) 12191–12200.
- [12] N. Mozaffari, T. Duong, M. Shehata, A.D. Bui, H.T. Pham, Y. Yin, Y.O. Mayon, J. Zheng, M.A. Mahmud, G.D. Tabi, Above 23% Efficiency by Binary Surface Passivation of Perovskite Solar Cells Using Guanidinium and Octylammonium Spacer Cations, *Solar RRL*, 2022.
- [13] Q. Wang, J.-E. Moser, M. Grätzel, Electrochemical impedance spectroscopic analysis of dye-sensitized solar cells, *J. Phys. Chem. B* 109 (2005) 14945–14953.
- [14] Y. Proskuryakov, K. Durose, M. Al Turkestani, I. Mora-Seró, G. Garcia-Belmonte, F. Fabregat-Santiago, J. Bisquert, V. Barrioz, D. Lamb, S. Irvine, Impedance spectroscopy of thin-film CdTe/CdS solar cells under varied illumination, *J. Appl. Phys.* 106 (2009), 044507.
- [15] M. Makhlof, M. Shehata, Improvement of photoresponse in an isatin hydrazone/CdTe hybrid heterostructure device via ZnO chelation for photovoltaic applications, *Sol. Energy* 211 (2020) 1128–1136.
- [16] I. Mora-Seró, Y. Luo, G. Garcia-Belmonte, J. Bisquert, D. Muñoz, C. Voz, J. Puigdollers, R. Alcubilla, Recombination rates in heterojunction silicon solar cells analyzed by impedance spectroscopy at forward bias and under illumination, *Sol. Energy Mater. Sol. Cell.* 92 (2008) 505–509.
- [17] O. Almora Rodríguez, L.G. Gerling, C. Voz Sanchez, R. Alcubilla, J. Puigdollers, G. Garcia-Belmonte, Superior Performance of V2O5 as Hole Selective Contact over Other Transition Metal Oxides in Silicon Heterojunction Solar Cells, 2017.
- [18] I. Mora-Seró, G. Garcia-Belmonte, P.P. Boix, M.A. Vazquez, J. Bisquert, Impedance spectroscopy characterisation of highly efficient silicon solar cells under different light illumination intensities, *Energy Environ. Sci.* 2 (2009) 678–686.
- [19] J. Panigrahi, R. Singh, N. Batra, J. Gope, M. Sharma, P. Pathi, S. Srivastava, C. Rauthan, P. Singh, Impedance spectroscopy of crystalline silicon solar cell: observation of negative capacitance, *Sol. Energy* 136 (2016) 412–420.
- [20] T. Yeow, J. Sun, Z. Yao, J.-N. Jaubert, K.P. Musselman, Evaluation of impedance spectroscopy as a tool to characterize degradation mechanisms in silicon photovoltaics, *Sol. Energy* 184 (2019) 52–58.
- [21] D.B. Sulas-Kern, M. Owen-Bellini, P. Ndione, L. Spinella, A. Sinha, S. Ulicna, S. Johnston, L.T. Schelhas, Electrochemical degradation modes in bifacial silicon photovoltaic modules, *Prog. Photovoltaics Res. Appl.* 30 (2022) 948–958.
- [22] D. Yan, A. Cuevas, J.I. Michel, C. Zhang, Y. Wan, X. Zhang, J. Bullock, Polysilicon passivated junctions: the next technology for silicon solar cells? *Joule* 5 (2021) 811–828.
- [23] J. Melskens, B.W. van de Loo, B. Macco, L.E. Black, S. Smit, W. Kessels, Passivating contacts for crystalline silicon solar cells: from concepts and materials to prospects, *IEEE J. Photovoltaics* 8 (2018) 373–388.
- [24] M. Shehata, P. Phang, R. Basnet, Y. Yin, F. Kremer, G. Bartholazzi, G.G. Andersson, D.H. Macdonald, L.E. Black, Outstanding surface passivation for highly efficient silicon solar cells enabled by innovative Al₂TiO₃/TiO₂ electron-selective contact stack, *Solar RRL*.
- [25] T.N. Truong, D. Yan, C. Samundsett, R. Basnet, M. Tebyetekerwa, L. Li, F. Kremer, A. Cuevas, D. Macdonald, H.T. Nguyen, Hydrogenation of phosphorus-doped polycrystalline silicon films for passivating contact solar cells, *ACS Appl. Mater. Interfaces* 11 (2019) 5554–5560.
- [26] F. Feldmann, C. Reichel, R. Müller, M. Hermle, The application of poly-Si/SiO_x contacts as passivated top/rear contacts in Si solar cells, *Sol. Energy Mater. Sol. Cell.* 159 (2017) 265–271.
- [27] H. Park, S. Bae, S.J. Park, J.Y. Hyun, C.H. Lee, D. Choi, D. Kang, H. Han, Y. Kang, H.-S. Lee, Role of polysilicon in poly-Si/SiO_x passivating contacts for high-efficiency silicon solar cells, *RSC Adv.* 9 (2019) 23261–23266.
- [28] A. Richter, R. Müller, J. Benick, F. Feldmann, B. Steinhauser, C. Reichel, A. Fell, M. Bivour, M. Hermle, S.W. Glunz, Design rules for high-efficiency both-sides-contacted silicon solar cells with balanced charge carrier transport and recombination losses, *Nat. Energy* 6 (2021) 429–438.
- [29] A.W. Blakers, A. Wang, A.M. Milne, J. Zhao, M.A. Green, 22.8% efficient silicon solar cell, *Appl. Phys. Lett.* 55 (1989) 1363–1365.
- [30] M.A. Green, The passivated emitter and rear cell (PERC): from conception to mass production, *Sol. Energy Mater. Sol. Cell.* 143 (2015) 190–197.
- [31] R. Basnet, S.P. Phang, C. Samundsett, D. Yan, W. Liang, C. Sun, S. Armand, R. Einhaus, J. Degoullange, D. Macdonald, 22.6% efficient solar cells with polysilicon passivating contacts on n-type solar-grade wafers, *Solar RRL* 3 (2019), 1900297.
- [32] T. Trupke, R. Bardos, M. Schubert, W. Warta, Photoluminescence imaging of silicon wafers, *Appl. Phys. Lett.* 89 (2006), 044107.
- [33] A. Bondarenko, G. Ragoisha, Progress in Chemometrics Research, Nova Science, New York, 2005, pp. 1110–1112, [abc.chemistry.bsu.by/vi/](http://www.bsu.by/vi/).
- [34] M. Makhlof, M. Shehata, Multilayer emitter of molybdenum oxide/silver/molybdenum oxide thin films for silicon heterojunction solar cells: device fabrication and electrical characterization, *J. Alloys Compd.* 904 (2022), 164102.
- [35] M. Makhlof, H. Khallaf, M. Shehata, Impedance spectroscopy and transport mechanism of molybdenum oxide thin films for silicon heterojunction solar cell application, *Appl. Phys. A* 128 (2022) 1–13.
- [36] R.A. Sinton, A. Cuevas, Contactless determination of current-voltage characteristics and minority-carrier lifetimes in semiconductors from quasi-steady-state photoconductance data, *Appl. Phys. Lett.* 69 (1996) 2510–2512.
- [37] B.G. Streetman, S. Banerjee, Solid State Electronic Devices, Pearson/Prentice Hall Upper, Saddle River, 2006.
- [38] K. Misiakos, D. Tsamakis, Accurate measurements of the silicon intrinsic carrier density from 78 to 340 K, *J. Appl. Phys.* 74 (1993) 3293–3297.
- [39] A. Schenk, Finite-temperature full random-phase approximation model of band gap narrowing for silicon device simulation, *J. Appl. Phys.* 84 (1998) 3684–3695.
- [40] V. Brus, On impedance spectroscopy analysis of nonideal heterojunctions, *Semicond. Sci. Technol.* 27 (2012), 035024.
- [41] S.M. Sze, Y. Li, K.K. Ng, Physics of Semiconductor Devices, John Wiley & sons, 2021.
- [42] J. Garland, D. Crain, J. Zheng, C. Sulyma, D. Roy, Electro-analytical characterization of photovoltaic cells by combining voltammetry and impedance spectroscopy: voltage dependent parameters of a silicon solar cell under controlled illumination and temperature, *Energy Environ. Sci.* 4 (2011) 485–498.
- [43] A. Braña, E. Forniés, N. López, B. García, High efficiency Si solar cells characterization using impedance spectroscopy analysis, in: *Journal of Physics: Conference Series*, IOP Publishing, 2015, 012069.
- [44] M.S. Abouzari, F. Berkemeier, G. Schmitz, D. Wilmer, On the physical interpretation of constant phase elements, *Solid State Ionics* 180 (2009) 922–927.
- [45] M. Shehata, M. Abdel-Hamed, K. Abdelhady, Structural and dielectric properties of Au/perylene-66/p-Si/Al hybrid heterojunction diode, *Vacuum* 151 (2018) 96–107.
- [46] P. Yadav, K. Pandey, B. Tripathi, M. Kumar, Investigation of interface limited charge extraction and recombination in polycrystalline silicon solar cell: using DC and AC characterization techniques, *Sol. Energy* 116 (2015) 293–302.
- [47] P. Yadav, K. Pandey, B. Tripathi, C.M. Kumar, S.K. Srivastava, P. Singh, M. Kumar, An effective way to analyse the performance limiting parameters of poly-crystalline silicon solar cell fabricated in the production line, *Sol. Energy* 122 (2015) 1–10.
- [48] D. Crain, J. Garland, S. Rock, D. Roy, Quantitative characterization of silicon solar cells in the electro-analytical approach: combined measurements of temperature and voltage dependent electrical parameters, *Anal. Methods* 4 (2012) 106–117.
- [49] M. Shehata, K. Abdelhady, Temperature and frequency dependence of dielectric relaxation and AC electrical conductivity in p-Si/CuPc hybrid photodiode, *Appl. Phys. A* 124 (2018) 1–13.
- [50] M. Shehata, M. Makhlof, H. Kamal, K. Abdelhady, Constructive impact of temperature and frequency on electrical transport performance of cobalt tetramethoxyphenylporphyrin/p-Si hybrid heterojunction solar cell, *J. Alloys Compd.* 796 (2019) 255–266.

Supporting data for:

Impedance Spectroscopy Characterization of c-Si Solar Cells with SiO_x/ Poly-Si Rear Passivating Contacts

Mohamed M. Shehata^{a,b*}, Thien N. Truong^a, Rabin Basnet^a, Hieu T. Nguyen^a, Daniel H. Macdonald^a, and Lachlan E. Black^{a*}

^aSchool of Engineering The Australian National University Canberra, ACT 2600, Australia

^bDepartment of Physics Faculty of Science Minia University El Minya City 61519, Egypt

mohamed.ismael@anu.edu.au

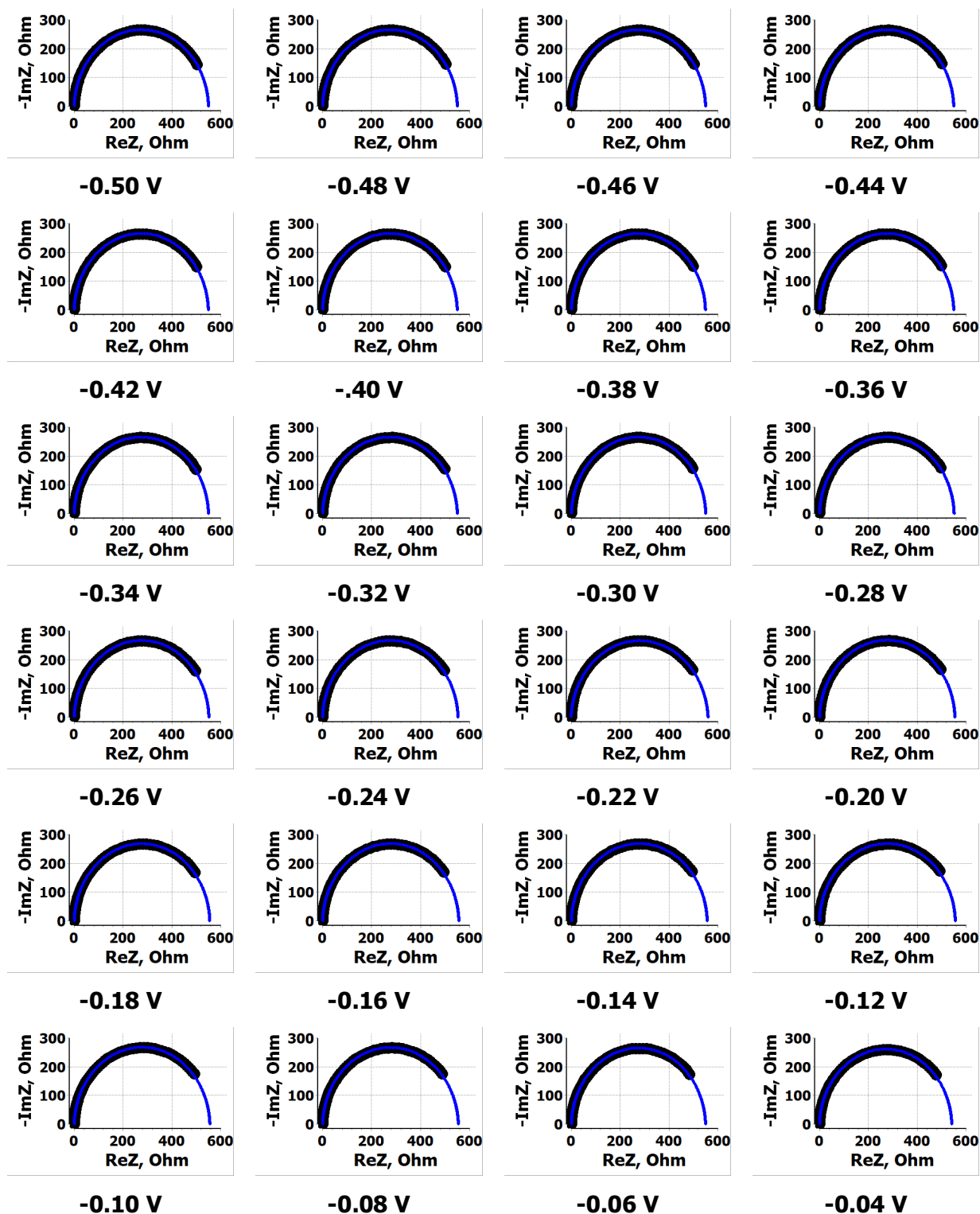
mohamed.shehata@mu.edu.eg

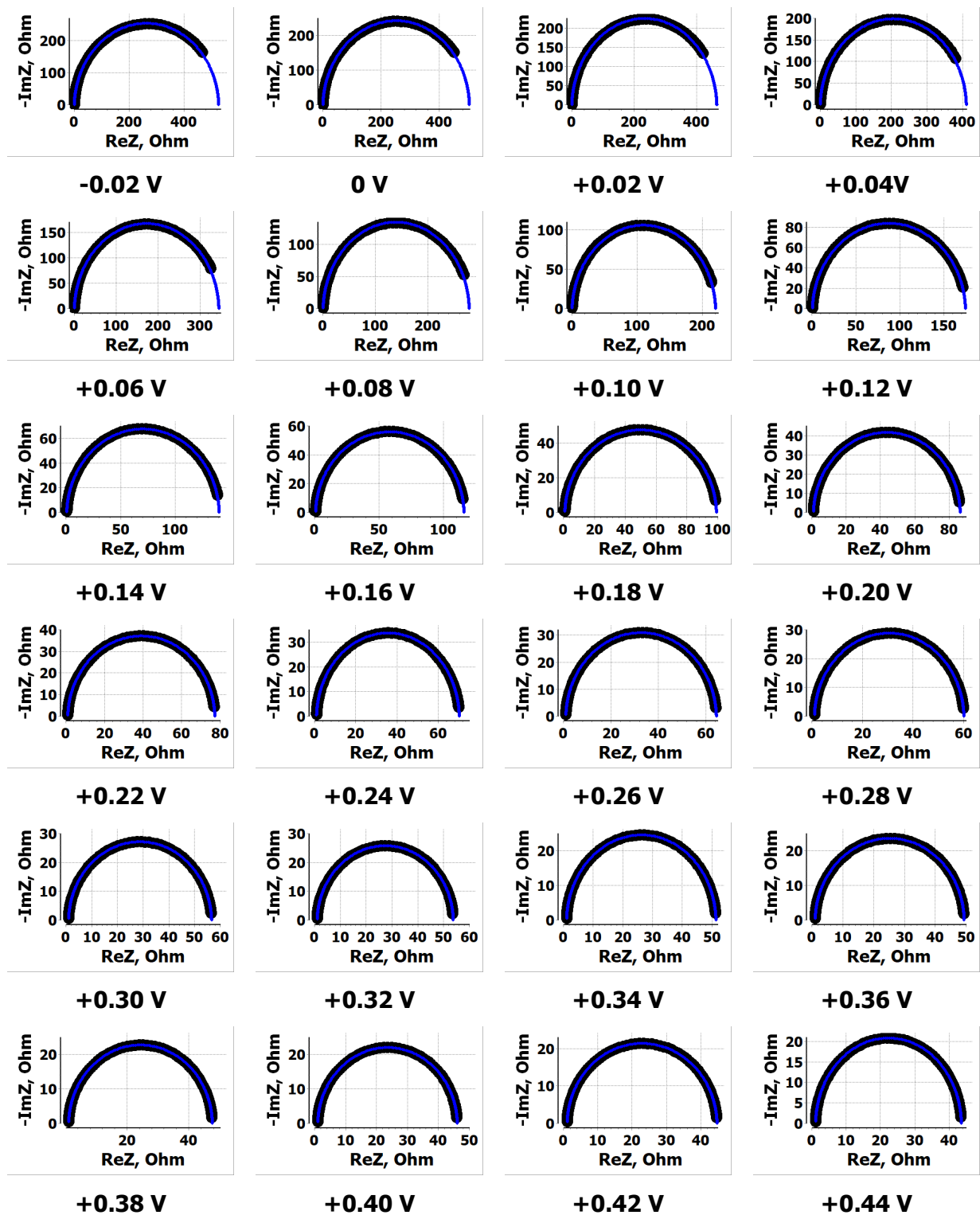
lachlan.black@anu.edu.au

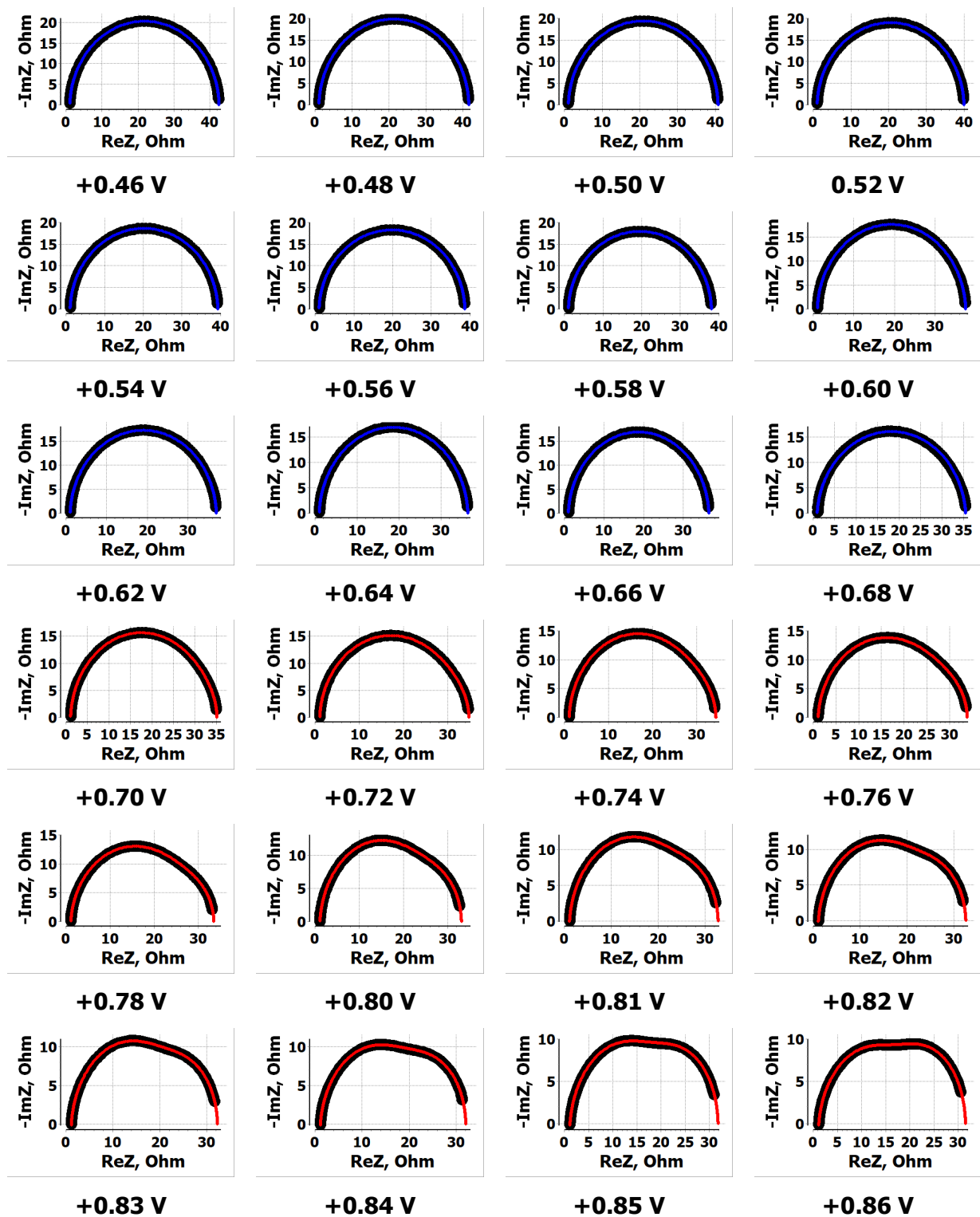
Discussion of band diagram

Fig. 1(b) shows the investigated c-Si solar cell's schematic band profile in thermal equilibrium (the cell has a single, constant-valued Fermi level). Due to the difference in doping concentration and doping type between the base and emitter regions a p-n junction is formed. The lightly doped base layer is the cell's thickest region that absorbs most of the incident light, resulting in generation of electron-hole pairs (EHPs). At equilibrium, electrons and holes flow from the n region to the p⁺ region and from the p⁺ region to the n region, respectively, and thus the space charge region (SCR) is established. These confined charges build up an electric field that prevents the normal flow of electrons and holes. The built-up electric field causes the energy bands to bend at the junction interface. Similarly, the low-high junction (LHJ) formed at the n-n⁺ interface induces a slight bending of the energy bands. Both n⁺ and p⁺ regions ensure that only one type of carrier can pass through them while the other type is blocked (carrier selectivity). The contact regions are highly doped junctions, the thicknesses of which are determined by balancing competing

requirements: providing lateral conduction and low contact resistivity, while minimising Auger recombination. Therefore, a proper doping profile in both the p^+ and the n^+ regions is necessary to achieve acceptable cell efficiency. In the energy band diagram for the metal contacts with n^+ region, an electrical Schottky potential barrier exists for moving an electron from the n^+ region into the metal. Analogously, in the p^+ case, an electrical potential barrier is encountered for moving a hole from the semiconductor into the metal. These Schottky barriers are due to the lower value of the work function of n^+ poly-Si, Φ_{n+} , than the work function of Ag, Φ_{Ag} , and the higher value of the work function of p^+ -Si, Φ_{p+} , than the work function of Cr, Φ_{Cr} . Since the n^+ and p^+ regions are heavily doped, the electrons and the holes will tunnel directly through these barriers, respectively. The values of depletion region width W_0 , Fermi energy E_F , barrier height ϕ_B , and built-in voltage V_{bi} presented in Fig. 1(b) are determined from the C–V measurements (discussed in detail in section 3.2). V_{bi} equals the difference between the work functions of the p^+ -Si and n -Si [1]; $V_{bi} = \Phi_{p+} - \Phi_n$, therefore $\Phi_{p+} = 5.00\text{eV}$ and $\Phi_n = 4.28\text{eV}$, where the electron affinity of Si $q\chi_{Si} = 4.05\text{eV}$ [1].







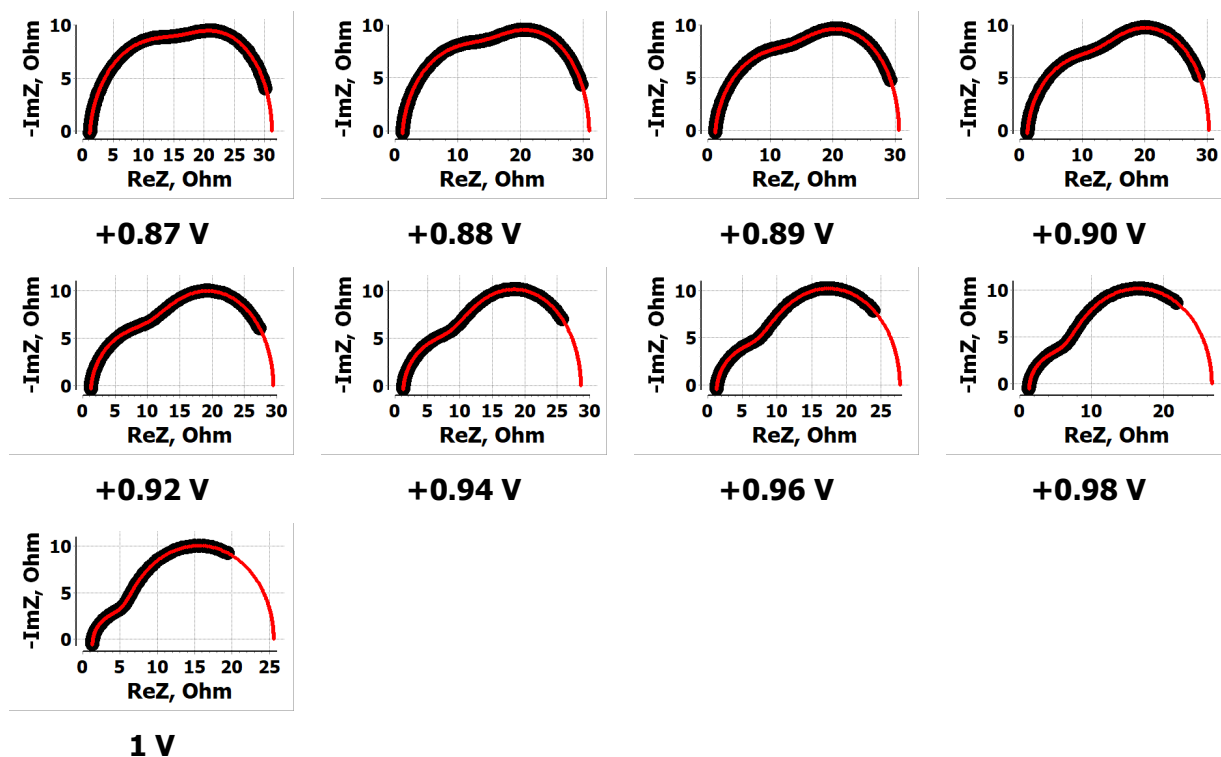


Fig. S1 Experimental Cole–Cole plots (black symbols) and their corresponding fits (solid blue/red lines) measured at 25°C as a function of applied DC voltages under dark, room-temperature conditions for the SiO_x/poly-Si rear passivating contact c-Si solar cell.

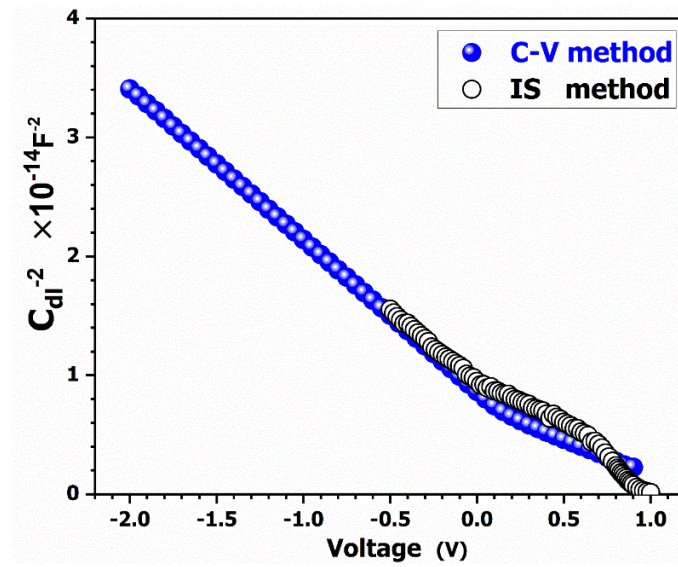


Fig. S2 Mott-Schottky plot comparison of data measured using either the single-frequency capacitance–voltage technique or impedance spectroscopy for the SiO_x /poly-Si rear passivating contact c-Si solar cell.

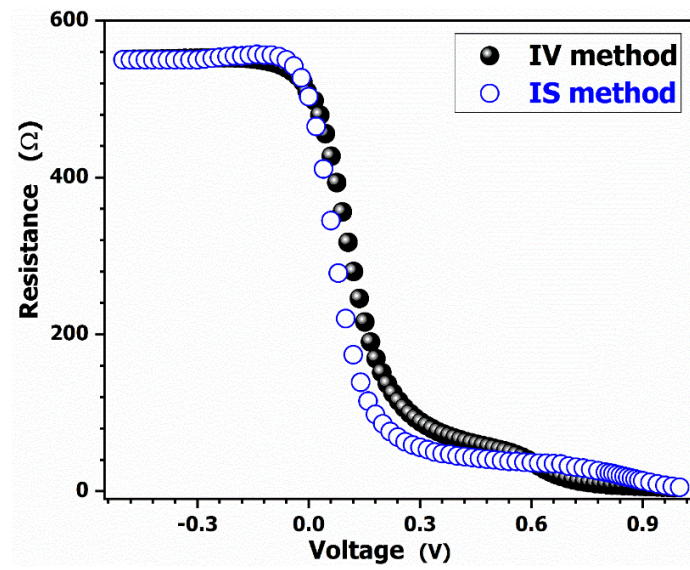


Fig. S3 Comparison of total resistance measured using the DC current–voltage (I–V) technique to that measured using impedance spectroscopy for the SiOx/poly-Si rear passivating contact c-Si solar cell.

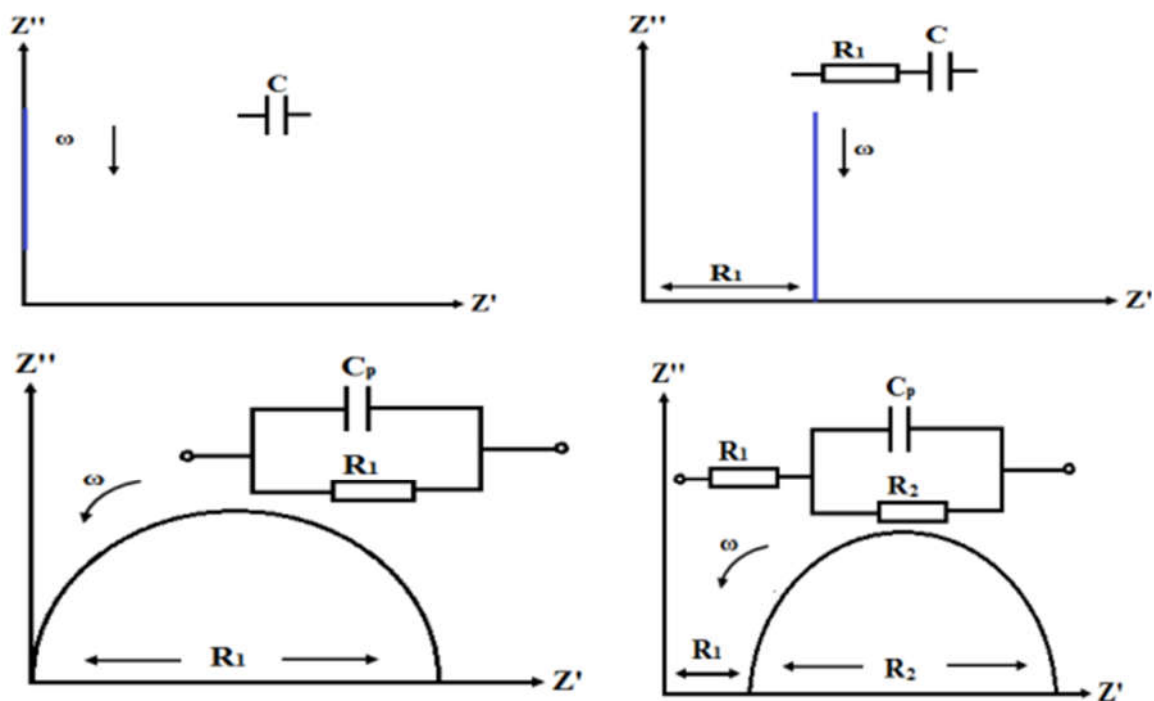


Fig. S4 Cole-Cole plots and their equivalent circuits of physical processes.

Reference

[1] Sharma, B. L., & Purohit, R. K. (2015). *Semiconductor heterojunctions* (Vol. 5). Elsevier.